



# Surface electric field driven directional charge separation on Ta<sub>3</sub>N<sub>5</sub> cuboids enhancing photocatalytic solar energy conversion

Chenguang Zhou<sup>a,1</sup>, Junkang Zhou<sup>b,1</sup>, Lei Lu<sup>a,1</sup>, Jiajia Wang<sup>c</sup>, Zhan Shi<sup>b</sup>, Bing Wang<sup>b</sup>, Lang Pei<sup>a</sup>, Shicheng Yan<sup>a,\*</sup>, Zhentao Yu<sup>a,\*</sup>, Zhigang Zou<sup>a,b</sup>

<sup>a</sup> Eco-Materials and Renewable Energy Research Center (ERERC), Collaborative Innovation Center of Advanced Microstructures, College of Engineering and Applied Sciences, Nanjing University, No. 22 Hankou Road, Nanjing, Jiangsu, 210093, PR China

<sup>b</sup> Jiangsu Key Laboratory for Nano Technology, National Laboratory of Solid State Microstructures, School of Physics, Nanjing University, No. 22 Hankou Road, Nanjing, Jiangsu, 210093, PR China

<sup>c</sup> College of Mechanics and Materials, Hohai University, Nanjing, 211100, PR China

## ARTICLE INFO

### Keywords:

Surface band bending  
Directional charge separation  
Ta<sub>3</sub>N<sub>5</sub>CO<sub>2</sub> reduction  
Photoelectrochemical water splitting

## ABSTRACT

Enhancing the separation and transfer of photogenerated carriers is critical factor for increasing the light to chemical energy conversion efficiencies. Here, we exposed {001} and {010} facets on [100] oriented Ta<sub>3</sub>N<sub>5</sub> cuboid, creating 18.6 times enhancement in photocatalytic reduction of CO<sub>2</sub> to CH<sub>4</sub> and a 0.42 V<sub>RHE</sub> (reference to reversible hydrogen electrode) photocurrent onset potential for photoelectrochemical water splitting. The pronounced photocatalytic performance is mainly attributed to that surface electric field from large surface band bending of the {001} with high work function drives electrons and holes to {010} and {001}, respectively, achieving a spatial charge separation. Differing to a main effect in charge separation and transfer for the traditional junction electric field region at buried heterojunction or homojunction interface, a surface electric field region is a place where charges separate and transfer efficiently and also the place for the catalytic reactions to occur.

## 1. Introduction

Using the photocatalysis technique to convert carbon dioxide into hydrocarbons or split water into hydrogen fuels is an economical strategy for solving environmental concerns and energy shortages [1,2]. To apply this technique, an efficient photocatalyst with visible-light absorption and high quantum efficiency is urgently needed for large-scale efficient conversion of solar energy into chemical energy [3–5]. Nevertheless, for many semiconductors with narrower band gaps, the low quantum efficiency remains a restriction in their practical applications owing to the high recombination of photogenerated carriers. Tantalum nitride (Ta<sub>3</sub>N<sub>5</sub>) photocatalyst with a band gap of 2.1 eV, absorbing a large proportion of the visible wavelength range of solar light (600 nm) with a theoretical solar-to-hydrogen (STH) conversion efficiency of 15.9%, is considered to be the promising candidate for photocatalytic and photoelectrochemical water splitting [6–9]. However, several unfavorable factors, such as both of heavy effective mass of photogenerated carriers and considerable crystal defects inducing unsatisfying separation and transfer of photogenerated carriers, severely constrained the photocatalytic performances regardless of the Ta<sub>3</sub>N<sub>5</sub>

powdered photocatalyst or photoanodes [10–12]. In order to improve the separation of photogenerated carriers, several accessible routes have been shown to be effective in reducing the charge recombination of Ta<sub>3</sub>N<sub>5</sub> such as forming the built-in electric field by constructing heterojunction with other semiconductors [13–16] or passivating the surface states with a passivation layer [17,18]. Nevertheless, restrictions on energy level matching in heterojunction or high-quality interface for effectively passivating the surface states are still the challenge to the development of high-activity Ta<sub>3</sub>N<sub>5</sub>.

Experimental and theoretical evidences have confirmed that 600 nm (2.06 eV) and 500 nm (2.48 eV) absorption edges coexist in the Ta<sub>3</sub>N<sub>5</sub> films, which can respectively be ascribed to photon absorption along a-axis and (b, c)-axes crystallographic directions [19], and a lighter carriers effective mass was found along (b, c)-axes directions in comparison with a-axis [20]. This means that overcoming the drawbacks of Ta<sub>3</sub>N<sub>5</sub> by constructing the a-axis oriented crystal structure, resulting in the shortened (b, c)-axes carriers migration distances, is highly reasonable to optimize the separation and transfer of carriers, thus enhancing the photocatalytic activity. Recently, much interest has been focused on semiconductor crystals with specific facets that induce the

\* Corresponding authors.

E-mail addresses: [yscfei@nju.edu.cn](mailto:yscfei@nju.edu.cn) (S. Yan), [yuzt@nju.edu.cn](mailto:yuzt@nju.edu.cn) (Y. Zhentao).

<sup>1</sup> These authors contributed equally to this work.

high reactive activities and high reactive selectivity [21]. It has been found that crystal facet engineering of several semiconductor metal oxides, such as  $\text{TiO}_2$  [22,23],  $\text{BiVO}_4$  [24–26],  $\text{SrTiO}_3$  [27],  $\text{CeO}_2$  [28], and  $\text{Cu}_2\text{O}$  [29], can achieve the anisotropic photogenerated charge transfer and accumulation, suppress carriers recombination, based on the different atomic construction and coordination between two adjacent facets. Attempts to deliberately fabricate such materials are challenged by the thermodynamic growth mechanisms of the crystals. Usually the selective adsorption of surfactants or ions on high-energy facets has been employed to suppress the growth rate along specific crystallographic direction [30]. However, the effects of  $\text{Ta}_3\text{N}_5$  crystal facet on the photocatalytic reactions were barely concerned, due to its harsh preparation conditions of high-temperature ammonolysis.

Herein, with assistance of NaCl–NaF eutectic molten salt, we have prepared a [100] crystallographic-direction growth  $\text{Ta}_3\text{N}_5$  cuboids with dominantly coexposed {001} and {010} crystal facets through the nitridation of  $\text{NaTaO}_3$  precursor. The  $\text{Ta}_3\text{N}_5$  cuboids exhibited a marked improvement in photocatalytic reduction of  $\text{CO}_2$  to  $\text{CH}_4$  and a 0.42  $V_{\text{RHE}}$  photocurrent onset potential for photoelectrochemical water splitting. The pronounced photocatalytic performance is mainly attributed to that a large surface band bending forms at the high-work-function {001} facet, which drives directional drift of electrons and holes to {010} and {001}, respectively, achieving a spatial charge separation. Differing to a main effect in charge separation for a buried junction electric field region of heterojunction, a surface electric field region under a crystal facet with high work function not only contributes to the charge separation and transfer but also offers the catalytic reaction sites. The proposed new strategy to combining the facet engineering and the oriented crystal growth may promote a rational material design for efficient solar energy conversion.

## 2. Experimental methods

### 2.1. Preparation of $\text{NaTaO}_3$ precursor

The  $\text{NaTaO}_3$  microcubes were prepared by a hydrothermal reaction. Typically,  $\text{Ta}_2\text{O}_5$  powder (1 mmol) was added to NaOH solution (30 mL, 1 M). After ultrasonic dispersion, the resultant suspension was poured into a 50 mL Teflon vessel and heated to 160 °C for 12 h. The obtained white powder was rinsed with deionized water thoroughly, and dried in an oven at 60 °C for 12 h.

### 2.2. Preparation of $\text{Ta}_3\text{N}_5$ samples

To synthesize [100] oriented  $\text{Ta}_3\text{N}_5$  cuboids, the obtained  $\text{NaTaO}_3$  microcubes were sufficiently mixed with NaCl–NaF (molar ratio of 2:1 for NaCl to NaF) mixed salts (molar ratio of 1:2 for  $\text{NaTaO}_3$  to molten salts) in a methanol, and subsequently calcined in air at 823 K for 2 h. The as-prepared  $\text{NaTaO}_3$ /NaCl–NaF powders (0.3 g) were heated at 1173 K for 7 h under flowing  $\text{NH}_3$  (800 mL·min<sup>−1</sup>). After natural cooling, the obtained product was washed several times with deionized water, and dried in an oven at 60 °C for 12 h. For comparison, using the same nitriding procedure, [100] oriented  $\text{Ta}_3\text{N}_5$  nanorods with no specific exposed facets was prepared by nitriding  $\text{NaTaO}_3$  microcubes (0.3 g) in NaCl molten salt (molar ratio of 1:2 for  $\text{NaTaO}_3$  to NaCl) and conventional  $\text{Ta}_3\text{N}_5$  particles were obtained by directly nitriding the  $\text{Ta}_2\text{O}_5$  precursors (0.3 g).

### 2.3. Sample characterizations

The phase structure of as-synthesized samples was measured with X-ray powder diffraction (XRD, Rigaku Ultima III) using Cu K $\alpha$  radiation at 40 kV and 40 mA. The size and morphology of samples were observed by scanning electron microscope (SEM, Nova NanoSEM 230FEI Co) and field emission transmission electron microscope (TEM, JEM-200CX). Ultraviolet-visible (UV–vis) diffuse reflectance spectra were

obtained by a UV–vis spectrophotometer (UV-2550, Shimadzu) and corresponding absorption spectra calculated by a Kubelka–Munk equation. The Brunauer–Emmett–Teller (BET) surface area was measured using a surface area analyser (Micromeritics Tristar-3000, USA) at liquid nitrogen temperature (77 K). The amounts of  $\text{CO}_2$  physisorbed on the  $\text{Ta}_3\text{N}_5$  samples were evaluated by BET method at ice water temperature (273 K). The constituent of samples was characterized by X-ray photoelectron spectroscopy (XPS, Thermo ESCALAB 250). Photoluminescence (PL) spectra were measured by using a picosecond Ti:Sapphire laser (Mira HP, from Coherent) as the excitation source. The decay profiles of  $\text{Ta}_3\text{N}_5$  samples were fitted by a biexponential function of  $I(t) = A_1 \exp(-t/\tau_1) + A_2 \exp(-t/\tau_2)$ , where  $I(t)$  is the fluorescence intensity at time  $t$ ,  $A_1$  and  $A_2$  are the pre-exponential factor, and  $\tau_1$  and  $\tau_2$  are the lifetime.

### 2.4. Facet-selective photodeposition of noble metals or/and metal oxides

Typically,  $\text{Ta}_3\text{N}_5$  powder (0.1 g), electron-reduced and/or hole-oxidized precursors with a 3Wt% weight ratio for products to  $\text{Ta}_3\text{N}_5$  were mixed in deionized water for obtaining 100 mL suspension. The suspension was irradiated by 300 W Xe lamp ( $\lambda \geq 420$  nm) with constant stirring for 5 h. The obtained products was filtered, washed with deionised water several times, and dried at 60 °C overnight. The photo-deposition of Pt, Au or Ag was carried out with  $\text{H}_2\text{PtCl}_6$  ( $\text{HAuCl}_4$ ,  $\text{AgNO}_3$ ) as precursor, and 20 mL methanol as hole sacrificial agent. The photo-deposition of  $\text{MnO}_x$  or  $\text{Co}_3\text{O}_4$  was carried out with  $\text{MnSO}_4$  ( $\text{Co}(\text{NO}_3)_2$ ) as the precursor, and  $\text{NaIO}_3$  (2.0 g) as electron acceptor. The simultaneous photo-reduction and photo-oxidation deposition were achieved with dual precursors without addition of additional electron acceptor or hole sacrificial agent.

### 2.5. Photocatalytic $\text{CH}_4$ evolution

Pt as a cocatalyst was loaded by following procedure.  $\text{Ta}_3\text{N}_5$  powders (0.1 g),  $\text{H}_2\text{PtCl}_6$  aqueous solution (3Wt% Pt, according to the weight ratio of Pt: $\text{Ta}_3\text{N}_5$ ) and  $\text{CH}_3\text{OH}$  solution (40 mL) were mixed in 60 mL deionized water. The suspension was then irradiated by 300 W Xe lamp ( $\lambda \geq 420$  nm) with magnetically stirring for 5 h. In the photocatalytic reduction of  $\text{CO}_2$ , the Pt-loaded  $\text{Ta}_3\text{N}_5$  powders (0.1 g) were homogeneously dispersed on a glass reactor with an area of 4.2 cm<sup>2</sup>. The volume of the reaction system was about 230 mL and a 300 W Xe lamp ( $\lambda \geq 420$  nm) was used as the light source for the photocatalytic reaction. After the reaction system was vacuum-treated several times, high-purity  $\text{CO}_2$  gas was introduced into the reaction to reach the ambient pressure. Deionized water (0.4 mL) was injected as a reducing agent into the reaction system. During irradiation, about 1 mL of gas was withdrawn from the reaction tank at a given interval and then subjected to  $\text{CH}_4$  concentration analysis using gas chromatography (GC-2014, Shimadzu Corp, Japan). The apparent quantum yields (AQYs) for  $\text{CO}_2$  reduction were measured using the same experimental process, except that a different cut-off filter (Y50, > 500 nm) was employed. The apparent quantum efficiency (AQY) was estimated by formula of

$$\text{AQY} = \frac{8 \times \text{number of } \text{CH}_4 \text{ molecules}}{\text{number of incident photons}} \times 100\% \quad (1)$$

The number of photons reaching the catalyst was measured using a spectroradiometer (LS-100, EKO Instruments Co., LTD.). It was assumed that all incident photons were absorbed by the catalyst. The total number of incident photons in the wavelength range of 500–600 nm was estimated to be  $2.36 \times 10^{21}$  photon·h<sup>−1</sup>.

### 2.6. Photoelectrochemical tests

The photoanodes were fabricated using an electrophoretic deposition (EPD) method followed by necking treatment. Typically, iodine (10 mg) and  $\text{Ta}_3\text{N}_5$  (40 mg) powders were dispersed in acetone (50 mL)

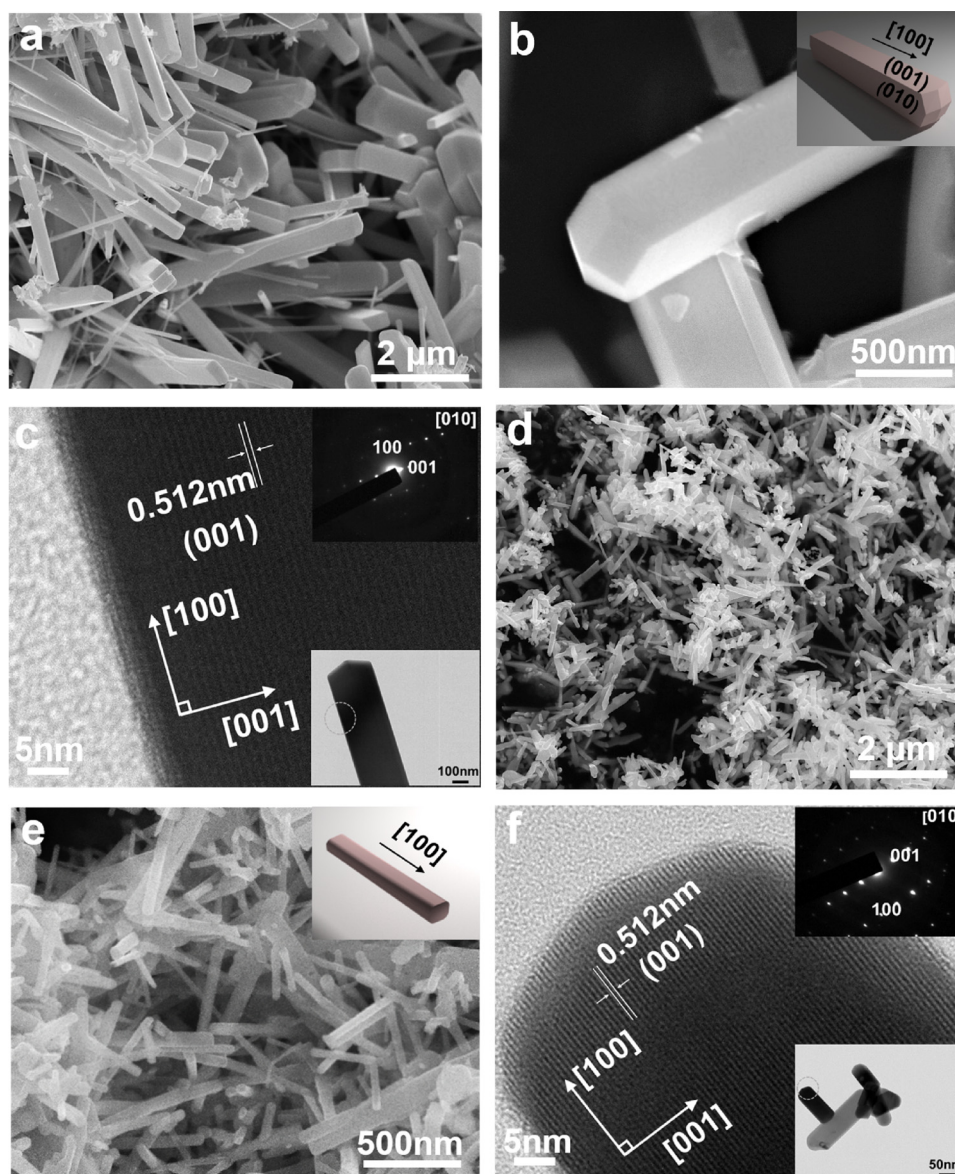


**Fig. 1.** SEM and HRTEM images for (a–c)  $\text{Ta}_3\text{N}_5$  cuboids and (d–f) nanorods. Insets in Fig. 1b and e show the schematic illustrations of cuboid and nanorod, respectively. TEM images of  $\text{Ta}_3\text{N}_5$  cuboids and nanorods, and their corresponding SAED patterns were shown in insets of Fig. 1c and f, respectively.

with the assistance of sonication to obtain the  $\text{Ta}_3\text{N}_5$  powder suspension for EPD. The EPD process for  $\text{Ta}_3\text{N}_5$  was conducted between two parallel FTO electrodes with the distance of 1 cm under 15 V of bias for 5 min. The average thickness of film on FTO was about 5  $\mu\text{m}$ , which was measured from the cross-sectional scanning electron microscopy image. The coated area of the  $\text{Ta}_3\text{N}_5$  films was ca. 1 cm  $\times$  1 cm. The electrodes were dried in air, and then dropped with  $\text{TaCl}_5$  methanol solution (10 mM, 10  $\mu\text{L}$ ) for five times. Finally, the dropped electrodes were heated at 500  $^\circ\text{C}$  for 30 min in flowing  $\text{NH}_3$  (500 mL  $\text{min}^{-1}$ ).

The deposition of Co species cocatalysts on  $\text{Ta}_3\text{N}_5$  photoanode was carried out by an impregnation method as the following procedures. The colloidal  $\text{Co}(\text{OH})_x$  solution was firstly prepared by the addition of NaOH solution (30  $\mu\text{L}$ , 1 M) into an aqueous solution of  $\text{Co}(\text{NO}_3)_2$  (5 mL, 0.01 M). The  $\text{Ta}_3\text{N}_5$  electrode was subsequently immersed into the as-prepared  $\text{Co}(\text{OH})_x$  colloidal solution for 1 h followed by washing with distilled water and then naturally dried in air at room temperature. Photoelectrochemical performance was measured in a three-electrode cell using an aqueous hydroxide electrolyte (1 M NaOH). A  $\text{Ta}_3\text{N}_5$  film, Ag/AgCl electrode and a Pt foil were used as working electrode, counter electrode and reference electrode, respectively. An

AM1.5 G sunlight simulator (100  $\text{mW cm}^{-2}$ , oriel 92251A-1000) was used as light source. Potentials of the working electrode were converted to a RHE (reversible hydrogen electrode) scale using the formula of  $V_{\text{RHE}} = V_{\text{Ag/AgCl}} + 0.0591 \text{ pH} + 0.1976 \text{ V}$ . The electrochemical analyzer (Solartron 1260 + 1287) was used to measure electrochemical impedance spectra under 10 mV amplitude perturbation and frequencies between 0.1 Hz and 10 MHz. Bulk charge separation efficiency ( $\eta_{\text{sep}}$ ) was calculated based on the equation:

$$J_{\text{Na}_2\text{SO}_3} = J_{\text{max}} \eta_{\text{abs}} \eta_{\text{sep}} \eta_{\text{trans}} \quad (2)$$

( $J_{\text{max}}$ : maximum theoretical photocurrent,  $\eta_{\text{abs}}$ : light absorption efficiency,  $\eta_{\text{trans}}$ : surface transfer efficiency). The  $\eta_{\text{trans}}$  was approximated as 100% when  $\text{Na}_2\text{SO}_3$  solution was used as an electrolyte. As a consequence, the photocurrent density in the presence of  $\text{Na}_2\text{SO}_3$  is obtained by:

$$J_{\text{Na}_2\text{SO}_3} = J_{\text{max}} \eta_{\text{abs}} \eta_{\text{sep}} \quad (3)$$

The corresponding charge separation efficiency:

$$\eta_{\text{sep}} = J_{\text{Na}_2\text{SO}_3} / (J_{\text{max}} \eta_{\text{abs}}) \quad (4)$$



## 2.7. Theoretical calculations

The DFT calculations are performed by the VASP code with the projected-augmented-wave (PAW) method. For the exchange-correlation functional, the generalized gradient approximation (GGA) in the scheme of Perdew-Bueke-Ernzerhof (PBE) is used. For N and Ta, the  $2s^2 3p^3$  and  $5p^6 5d^4 6s^1$  orbital, respectively, are treated as valence states. The cutoff energy for basis functional is 500 eV. The  $Ta_3N_5$  (010) and (001) surfaces can be exposed by different terminations. The slab models used in this work have been proved to be the most stable terminations. For the (010) and (001) surfaces, the  $\Gamma$ -centered k-point meshes of  $2 \times 6 \times 1$  and  $5 \times 5 \times 1$ , respectively, are adopted for the Brillouin zone integration. In addition, a stable structure to describe the oxygen atom replacing the nitrogen atom is estimated by calculating surface energies, and the most reliable slab model with  $O_N$  impurities is adopted.

## 3. Results and discussion

### 3.1. Flux-assisted nitridation route to $Ta_3N_5$ cuboids

$Ta_3N_5$  cuboids growing along the [100] crystallographic direction with exposed {010} and {001} facets were synthesized by nitriding  $NaTaO_3$  microcubes in eutectic molten salt of NaCl and NaF under flowing  $NH_3$  ( $800 \text{ mL min}^{-1}$ ) at 1173 K for 7 h. For comparison, using the same procedure, [100] oriented  $Ta_3N_5$  nanorods with no specific exposed facets were prepared by nitriding  $NaTaO_3$  microcubes in NaCl molten salt and conventional  $Ta_3N_5$  particles were obtained by directly nitriding the  $Ta_2O_5$  precursors. X-ray photoelectron spectroscopy (XPS) analysis (Fig. S1) indicated that the molten salt can be facilely eliminated by subsequent distilled water washing [31]. The Ta 4f XPS spectra were deconvoluted into four peaks: 26.0 eV for Ta 4f 5/2 and 24.2 eV for Ta 4f 7/2 in  $Ta_3N_5$ , and 27.2 eV for Ta 4f 5/2 and 25.4 eV for Ta 4f 7/2 in  $TaO_x$  species (Fig. S1a) [32,33]. Obviously, amount of  $TaO_x$  species is higher for the  $Ta_3N_5$  particles than  $Ta_3N_5$  nanorods and cuboids. This is attributed to the fact that replacing  $NaTaO_3$  by  $Ta_2O_5$  as precursor in the synthesis of  $Ta_3N_5$  will introduce more  $TaO_x$  species. As shown in Fig. 1a, b and S2a, the cuboid-like  $Ta_3N_5$  crystal was about 5–10  $\mu\text{m}$  in length and 400 nm in cross-section width. High-resolution transition electron microscope (HRTEM) images (Fig. 1c) showed that the spacing of lattice fringes paralleled to the longitudinal direction of  $Ta_3N_5$  cuboid to be 0.512 nm, which can be assigned to the lattice pitch of (001) atomic plane [34,35]. Selected area electron diffraction (SAED) (inset of Fig. 1c) indicates that the cuboid is a uniform single crystal with the longitudinal direction along [100] and the width direction along [010] and [001]. The two major exposed surfaces of the cuboid were accordingly determined to be {010} and {001} facets. Comparatively, nitriding  $NaTaO_3$  microcubes in NaCl molten salt, the final product is [100] oriented  $Ta_3N_5$  nanorods with uniform size of  $\sim 500 \text{ nm}$  in length and  $\sim 20 \text{ nm}$  in diameter (Fig. 1d–f). No clear facet-exposed structure in  $Ta_3N_5$  nanorods was observed by scanning electron microscope (SEM) images (Fig. 1d, e and S2b). As demonstrated in previous reports,  $Ta_3N_5$  particles with unknown crystal orientation could be formed by directly heating  $NaTaO_3$  microcube layers coated on the Ta metal substrate at 1073 K in  $NH_3$  flow [18,36,37]. In our case, addition of the molten salts, which induces a solvent effect during initial dissolution of mother-crystal  $NaTaO_3$  particles and subsequent recrystallization, is favorable to the a-axis oriented growth of  $Ta_3N_5$  nanorods. Furthermore, compared with individual NaCl molten salt (melting point at 1074 K), the eutectic NaCl–NaF molten salt (melting point at 923 K) with lower melting point is favorable for stabilizing high-energy {010} and {001} facets, probably due to that the sufficient solvent environment facilitates the crystal growth and the co-adsorption of F and Cl species strongly changes the surface energy during the crystal growth in molten salt [38].

The X-ray diffraction (XRD) patterns of these as-prepared  $Ta_3N_5$

samples were indexed to the single-phase orthorhombic structural  $Ta_3N_5$  (JCPDS No. 19-1291) (Fig. S3). Notably, the diffraction intensity of (023) facet for  $Ta_3N_5$  cuboids and nanorods was obviously higher than that of conventional  $Ta_3N_5$  particles, suggesting that both the cuboids and nanorods were [100] oriented  $Ta_3N_5$  crystal [19]. UV–vis absorption measurements (Fig. S4) indicated that the  $Ta_3N_5$  cuboids, nanorods and particles have same absorption edge to be 600 nm, originating from the band gap excitation from N 2p orbitals to Ta 5d orbitals. Indeed, a slight step absorption is clearly visible at about 500 nm in the UV/Vis absorption spectra for [100] oriented  $Ta_3N_5$  nanorods and cuboids, due to the prominent optical anisotropy in a-axis dominant  $Ta_3N_5$  crystals [19]. An absorption peak was observed in 650–800 nm, resulting from the reduced tantalum defects [39]. Intensity of the defect absorption peak slightly decreased for both  $Ta_3N_5$  cuboids and nanorods than particles, indicating that the molten salt growth is beneficial to reduce the crystal defects.

### 3.2. Photoreduction of $CO_2$ into $CH_4$ over $Ta_3N_5$ cuboids

The photocatalytic activities of these as-synthesized  $Ta_3N_5$  cuboids, nanorods and particles with and without 3Wt% Pt cocatalyst were estimated by photoreduction of  $CO_2$  under the irradiation of a 300 W Xe lamp with a cut-off filter ( $\lambda \geq 420 \text{ nm}$ ). As shown in Fig. 2a,  $Ta_3N_5$  cuboids exhibited the highest  $CH_4$  generation rate to be  $0.141 \mu\text{mol h}^{-1}$ , about 2.8 and 6.4 times higher than  $0.051 \mu\text{mol h}^{-1}$  for  $Ta_3N_5$  nanorods and  $0.022 \mu\text{mol h}^{-1}$  for  $Ta_3N_5$  particles, respectively. A  $CO_2$  reduction experiment performed in the dark or in the absence of the photocatalyst showed no appearance of  $CH_4$ , proving that the  $CO_2$  reduction reaction is driven by light with the photocatalyst.  $^{13}C$  isotope labeling was performed by GC–MS after irradiation of  $Ta_3N_5$  under  $^{13}CO_2$  atmosphere for 7 h. As shown in Fig. S5, clear  $^{13}CH_4$  signal was observed in gaseous products, meaning that the  $CH_4$  is indeed generated by  $CO_2$  reduction. After deposition of the Pt by photoreduction, the  $CH_4$  generation rate over  $Ta_3N_5$  cuboids reached up to  $0.652 \mu\text{mol h}^{-1}$ , which is 3.7 and 18.6 times higher than  $Ta_3N_5$  nanorods ( $0.175 \mu\text{mol h}^{-1}$ ) and particles ( $0.035 \mu\text{mol h}^{-1}$ ), respectively. The  $O_2$  evolution rate was  $1.31 \mu\text{mol h}^{-1}$ , close to 2:1 M ratio of  $O_2$  to  $CH_4$ , and very small amount of CO ( $< 0.02 \mu\text{mol g}^{-1}$ ) and  $N_2$  ( $< 0.1 \mu\text{mol g}^{-1}$ ) were detected at the initial stage, which may be derived from the decomposition of the sample surface adsorption species. As described in the previous reports, the  $CH_4$  is the observed main product for the gaseous  $CO_2$  reduction reaction [40,41]. This is probably attributed to that the  $CH_4$  is the most stable product, as well demonstrated in the degradation of alkane. In the case of degradation of alkane, a mixture of five different hydrocarbons  $CH_4$ ,  $C_2H_4$ ,  $C_2H_6$ ,  $C_3H_6$ , and  $C_3H_8$  was exposed to the photocatalyst in the presence of light and water vapor [3]. After 120 min of illumination, the hydrocarbons except  $CH_4$  degraded significantly. This indicated that the  $CH_4$  is more stable during the gaseous photocatalytic reaction. Other products such as the  $HCOOH$  or  $H_2$  were usually observed during the  $CO_2$  reduction on an electrode in liquid media due to the separated oxidation and reduction reaction chamber by proton exchange member [42]. However, for gaseous photocatalytic reaction, the oxidation and reduction reactions occur in the same reaction chamber, in which metastable reduced products were oxidized easy.

The apparent quantum yields (AQYs) of  $Ta_3N_5$  particles, nanorods and cuboids photo-loaded with the Pt cocatalyst (3Wt%) were estimated to be 0.06%, 0.3% and 1.1% at 500 nm, respectively. This confirms a fact that the  $Ta_3N_5$  cuboids present a high activity in  $CO_2$  reduction. The specific surface area was determined by Brunauer–Emmett–Teller (BET) method to be  $11.1 \text{ m}^2 \text{ g}^{-1}$  for  $Ta_3N_5$  particles, about 2 times higher than  $5.4 \text{ m}^2 \text{ g}^{-1}$  for  $Ta_3N_5$  cuboids and  $6.6 \text{ m}^2 \text{ g}^{-1}$  for  $Ta_3N_5$  nanorods. This indicated that the difference in photocatalytic performance among the three  $Ta_3N_5$  samples can not be attributed to the difference in specific surface area. The amount of  $CO_2$  physisorbed on the  $Ta_3N_5$  cuboids was evaluated by BET method at 273 K to be

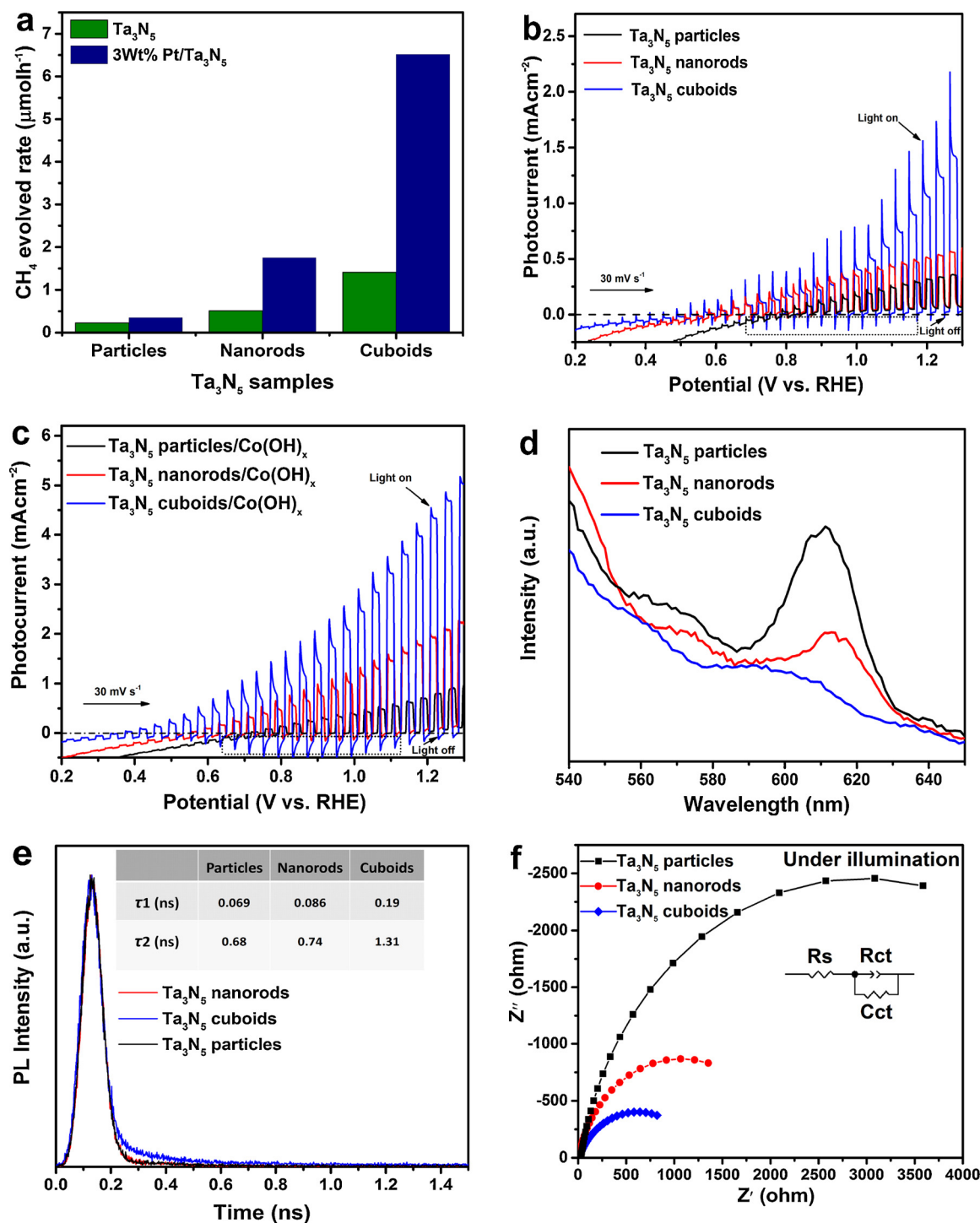


**Fig. 2.** (a) Photocatalytic  $\text{CO}_2$  reduction tests for the various  $\text{Ta}_3\text{N}_5$  samples without and with loading of 3Wt% Pt under visible light irradiation ( $\lambda \geq 420 \text{ nm}$ ). Light source: 300 W Xenon lamp. Photocatalysts: 0.1 g. (b, c) Current-potential curves for the various  $\text{Ta}_3\text{N}_5$  electrodes without and with the modification of  $\text{Co(OH)}_x$ . (d) Photoluminescence spectra of synthesized  $\text{Ta}_3\text{N}_5$  samples with an excitation wavelength of 450 nm. (e) Time-resolved transient PL decay of  $\text{Ta}_3\text{N}_5$  samples. (f) Electrochemical impedance (EIS) analysis of the as-prepared  $\text{Ta}_3\text{N}_5$  samples under UV-vis light illumination (300 W Xe lamp). Inset shows the equivalent circuit.  $R_s$ ,  $R_{ct}$ , and  $C_{ct}$  are the resistance from electrolyte and semiconductor-substrate electrical connection, interfacial charge transfer resistance between semiconductor and electrolyte, and the circuit capacitance, respectively.

$0.31 \text{ mg m}^{-2}$ , which is similar to  $0.29 \text{ mg m}^{-2}$  for  $\text{Ta}_3\text{N}_5$  nanorods and is about 3 times higher than  $0.11 \text{ mg m}^{-2}$  for  $\text{Ta}_3\text{N}_5$  particles, respectively (Fig. S6 and Table S1). Therefore, preferential adsorption of  $\text{CO}_2$  and low defect states for flux-assisted grew  $\text{Ta}_3\text{N}_5$  cuboids and nanorods may contribute to their higher  $\text{CO}_2$  reduction ability than  $\text{Ta}_3\text{N}_5$  particles. However, the similar adsorption of  $\text{CO}_2$  and defect density on  $\text{Ta}_3\text{N}_5$  cuboids and nanorods can not induce their big performance

differences in  $\text{CH}_4$  generation.

### 3.3. Photoelectrochemical tests showing the separation efficiency of $\text{Ta}_3\text{N}_5$ cuboids

In order to further discover the nature of enhancement in photocatalytic performance of  $\text{Ta}_3\text{N}_5$  cuboids, the three as-prepared  $\text{Ta}_3\text{N}_5$

samples were respectively deposited on the fluorine-doped tin oxide (FTO) substrate using electrophoretic (EP) deposition technique with post-necking treatment with  $\text{TaCl}_5$  to form effective contacts between the  $\text{Ta}_3\text{N}_5$  crystal particles [43]. The as-prepared  $\text{Ta}_3\text{N}_5$  photoanodes were then evaluated for photoelectrochemical water splitting in 1 M NaOH electrolyte (pH 13.6). As shown in Fig. 2b, the anodic photocurrents of  $\text{Ta}_3\text{N}_5$  cuboids, nanorods and particles were observed at around 0.67, 0.66 and 0.86  $V_{\text{RHE}}$ , and reached 1.37, 0.54 and 0.32  $\text{mA cm}^{-2}$  at 1.23  $V_{\text{RHE}}$ , respectively. After depositing  $\text{Co(OH)}_x$  as water oxidation cocatalyst (Fig. S7), the detected anodic photocurrents of  $\text{Ta}_3\text{N}_5$  cuboids/ $\text{Co(OH)}_x$  and  $\text{Ta}_3\text{N}_5$  nanorods/ $\text{Co(OH)}_x$  were about 5 and 2.2 times increase than that of  $\text{Ta}_3\text{N}_5$  particles/ $\text{Co(OH)}_x$  (0.94  $\text{mA cm}^{-2}$  at 1.23  $V_{\text{RHE}}$ ), reaching 4.68 and 2.11  $\text{mA cm}^{-2}$  at 1.23  $V_{\text{RHE}}$ , respectively (Fig. 2c). And the photocurrent onset potential of cuboid/ $\text{Co(OH)}_x$  electrode shifted to 0.42  $V_{\text{RHE}}$ , which is much lower than 0.75  $V_{\text{RHE}}$  for  $\text{Ta}_3\text{N}_5$  particles/ $\text{Co(OH)}_x$  and 0.61  $V_{\text{RHE}}$  for the nanorods/ $\text{Co(OH)}_x$ . Generally, the high onset potential can be attributed to many factors, such as the unsatisfying light absorption, low interfacial charge injection efficiency and the inefficient carrier separation and transport. In our case, the water oxidation cocatalyst,  $\text{Co(OH)}_x$ , was used to improve the charge injection efficiency [7,8], and there are no obvious differences in the light absorption between the nanorods and cuboids (Fig. S4). The bulk charge separation efficiency ( $\eta_{\text{sep}}$ ) was measured in 0.1 M  $\text{Na}_2\text{SO}_3$  solution (pH was buffered to 7.5) (Fig. S8), both  $\text{Ta}_3\text{N}_5$  electrodes with and without modification of  $\text{Co(OH)}_x$  presented an obvious order of cuboids > nanorods > particles. In a wide potential range of 0.6–1.2  $V_{\text{RHE}}$ , charge separation efficiency of cuboids is about 2 times higher than that of nanorods. Meanwhile, in order to exclude the  $\text{TaCl}_5$  in the process of necking treatment may affect the spatial charge separation of the particle itself. The photocurrent activities over the various  $\text{Ta}_3\text{N}_5$  electrodes were estimated without necking treatment and with  $\text{TiCl}_4$  treated, respectively (Fig. S9). The same change trend between  $\eta_{\text{sep}}$  and photocurrent activity probably meaning that the high activity of  $\text{Ta}_3\text{N}_5$  cuboids would originate from their high charge separation efficiency.

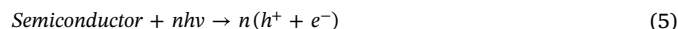
It is noteworthy that the cross-section width of  $\text{Ta}_3\text{N}_5$  cuboids is about 20 times larger than the diameter of  $\text{Ta}_3\text{N}_5$  nanorods (Fig. 1b, e). Under the back-side (from FTO, holes travel through the semiconductor layer to semiconductor-liquid interface) and front-side illumination (from semiconductor, electrons travel through the semiconductor layer to FTO substrate) on  $\text{Ta}_3\text{N}_5$  cuboids or nanorods electrode, no obvious photocurrent difference was observed, revealing an excellent charge transfer among these crystals (Fig. S10). Therefore, the enhanced activity for  $\text{Ta}_3\text{N}_5$  cuboids than nanorods can not be attributed to the decreased grain boundaries in the  $\text{Ta}_3\text{N}_5$  cuboids electrode with big crystal size. The electrochemical active surface area (ECSA) was estimated by using electrocapacitive measurements (Fig. S11).  $\text{Ta}_3\text{N}_5$  nanorods and cuboids electrodes show similar ECSA, and are both lower than  $\text{Ta}_3\text{N}_5$  particles, which is in good agreement with the BET measurements. According to the formula  $a = B_i(h\nu - E_g)^2/h\nu$  ( $a$  is the absorption coefficient,  $h\nu$  is the incident photon energy, and  $B_i$  is the absorption constant), the band gaps of  $\text{Ta}_3\text{N}_5$  particles, nanorods and cuboids are estimated to be 2.06 eV (Fig. S12a). The valence band maximum of the three  $\text{Ta}_3\text{N}_5$  samples are measured to be similar (Fig. S12b), thus the synthesized  $\text{Ta}_3\text{N}_5$  samples with different structures have the same conduction band minimum and valence band maximum. The photoluminescence (PL) spectra revealed that the  $\text{Ta}_3\text{N}_5$  cuboids exhibited the lower band edge recombination with an emission peak at about 610 nm than  $\text{Ta}_3\text{N}_5$  nanorods and particles (Fig. 2d), probably meaning that either the longer lifetime of the photogenerated charges with the slower recombination process or shorter lifetime of the photogenerated charges with the faster migration process. As seen in Fig. 2e, the PL decay curves of these samples were mathematically fitted by a biexponential model (Supporting information for details). In the inset table of Fig. 2e, the short lifetime  $\tau_1$  is usually attributed to the nonradiative recombination of the free excitations with surface defects,

and the long lifetime  $\tau_2$  is assigned to the radiative pathway from the recombination of photogenerated electrons and holes [44]. Relative to the  $\text{Ta}_3\text{N}_5$  particles ( $\tau_2 = 0.68$  ns) and nanorods ( $\tau_2 = 0.74$  ns), the transient PL decay trace of the  $\text{Ta}_3\text{N}_5$  cuboids demonstrates that PL lifetime ( $\tau_2$ ) is prolonged to  $\sim 1.31$  ns, indicating that the crystal facet exposure on  $\text{Ta}_3\text{N}_5$  cuboid may present strong positive association with its high charge separation ability which restrains the recombination of charges, achieving the longer survival time of the charges. Indeed, electrochemical impedance spectroscopy (EIS) measurement under irradiation showed an obvious decrease in semicircle diameter for cuboids than nanorods, indicating that the  $\text{Ta}_3\text{N}_5$  cuboids have more excellent electrical conductivity due to the promoted charge separation and transfer (Fig. 2f).

#### 3.4. Photodeposition to visualize the directional charge transfer

To further confirm the charge spatial separation, selective photodeposition of cocatalysts were also performed. The effect of directional charge transfer was verified based on the following mechanisms [24,26]:

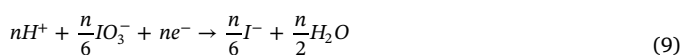
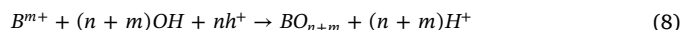
The generation of photo-induced carriers,



For photoreduction deposition,



For photooxidation deposition,



Where, A is the noble metal (Pt, Ag, Au...) for reduction and B is the metal (Mn, Co...) for oxidation.

Photoreduction deposition of Pt particles for visualizing the electron transfer demonstrated that a majority of Pt particles were evidently deposited on the two symmetric surfaces among four exposed facets of  $\text{Ta}_3\text{N}_5$  cuboid. Contrarily, photooxidation deposition of  $\text{MnO}_x$  to visualize the hole transfer mainly distributed on the another two symmetric surfaces of cuboid. A codeposition experiment indicated that  $\text{MnO}_x$  and Pt particles were respectively formed on two adjacent facets (Fig. S13). When using  $\text{Au}^{3+}$  and  $\text{Co}^{2+}$  to replace  $\text{Pt}^{4+}$  and  $\text{Mn}^{2+}$ , respectively, similar experimental phenomena were still observed, further indicating that the light-driven selective deposition does not depend on the type of ion precursors (Fig. 3). These evidences proved that the photogenerated carriers selectively accumulated on the specific facets. Effective mass of electrons and holes towards [010] and [001] directions has been calculated, respectively, and demonstrated a slight difference in their mobility [20]. Therefore, the directional charge transfer can not be attributed to the difference in charge mobility.

#### 3.5. The nature of spatial charge separation in $\text{Ta}_3\text{N}_5$ cuboids

Surface potential distribution on two adjacent facets of  $\text{Ta}_3\text{N}_5$  cuboid was detected by using Kelvin probe force microscope (KPFM) to measure contact potential difference (CPD) between a conducting tip and the sample [45]. Therefore, for a semiconductor, the CPD is defined as

$$V_{\text{CPD}} = (\phi_{\text{sample}} - \phi_{\text{tip}})/e \quad (10)$$

(where  $\phi_{\text{sample}}$  and  $\phi_{\text{tip}}$  are the work functions of the sample and tip, and  $e$  is the electronic charge), would be related to the space charge regions beneath the surfaces. As shown in Fig. 4, it is obvious that there is a more positive surface potential on a facet of  $\text{Ta}_3\text{N}_5$  cuboid than its



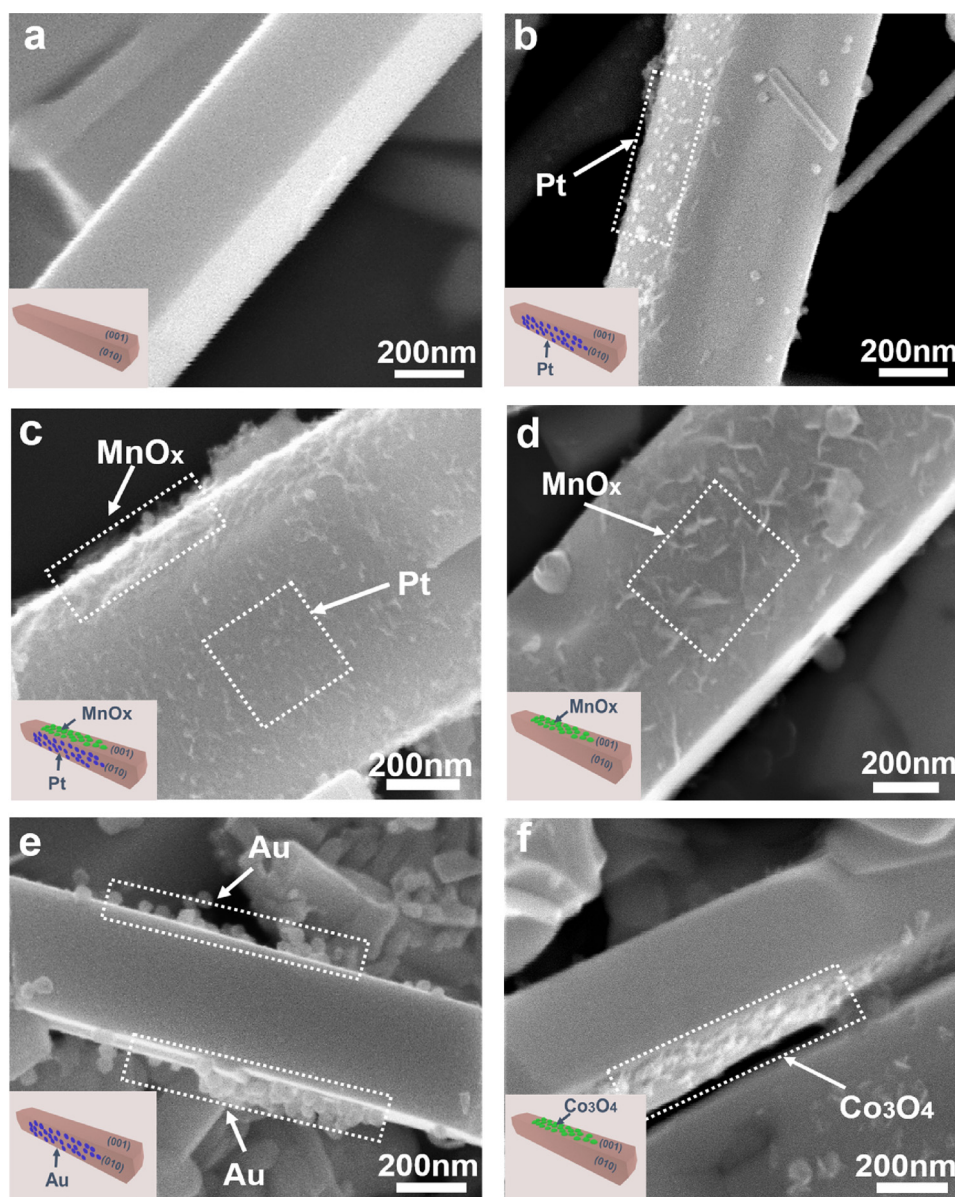


**Fig. 3.** SEM images for  $\text{Ta}_3\text{N}_5$  cuboids with and without cocatalysts photodeposited. (a)  $\text{Ta}_3\text{N}_5$ , (b)  $\text{Pt}/\text{Ta}_3\text{N}_5$ , (c)  $\text{Pt-MnO}_x/\text{Ta}_3\text{N}_5$ , (d)  $\text{MnO}_x/\text{Ta}_3\text{N}_5$ , (e)  $\text{Au}/\text{Ta}_3\text{N}_5$  and (f)  $\text{Co}_3\text{O}_4/\text{Ta}_3\text{N}_5$ .

adjacent side facet. This implies that the two adjacent facets exhibited the different surface work functions, thus inducing the different surface band bending for the ideal surface. As a consequence, it is reasonably suggested that the fabricated crystal-facet architecture was potentially responsible for the unusual enhancement in charge separation efficiency of  $\text{Ta}_3\text{N}_5$  cuboids.

The theoretical simulations revealed that a stable (010) and (001) surface on orthorhombic  $\text{Ta}_3\text{N}_5$  was composed of the N-Ta tetrahedron and octahedron units, respectively. As can be seen in the slab models of the {010} and {001} surfaces (Fig. S14), the surface atomic construction of {001} is flatter than that of {010}, and N atoms on the top layer of the {010} surfaces are all five-coordinated in contrast to {001} surfaces with only 50% five-coordinate N atoms. As demonstrated in our previously theoretical and experimental results [46–48], inevitable surface oxygen-related defects naturally occur during the synthetic process of  $\text{Ta}_3\text{N}_5$  due to its thermodynamic instability. Indeed, X-ray photoelectron spectroscopy confirmed that lattice oxygen with about 0.3:1 atomic ratio of O to Ta exists on the surface of  $\text{Ta}_3\text{N}_5$ , maybe locate at the nitrogen sites ( $\text{O}_\text{N}$ ) (Table S2). Density functional theory

(DFT) calculations on the slab models of {001} +  $\text{O}_\text{N}$  and {010} +  $\text{O}_\text{N}$  surfaces indicated that introduction of the  $\text{O}_\text{N}$  makes the Fermi level in the band gap of clean {010} surface moves to the conduction band of {010} +  $\text{O}_\text{N}$  surface and the Fermi level at valence band of {001} surface enter band gap of {001} +  $\text{O}_\text{N}$  (Fig. 5a and S15). Generally, owing to an extremely low defect transition energy, the  $\text{O}_\text{N}$  impurities as the electron donors is able to reduce Ta, resulting in the conduction band downshift for {010} +  $\text{O}_\text{N}$  than {010} facet. However, no obvious conduction band shift was observed for {001} +  $\text{O}_\text{N}$  referring to {001} facet. This is because that the electrons donated by  $\text{O}_\text{N}$  have been compensated by the surface states of {001} +  $\text{O}_\text{N}$  and no more electrons can reduce the Ta atoms, as indicated by that the surface states of the clean {001} surface is located above the Fermi level.

Oxygen impurities changing the electronic structures of {010} and {001} facets also affects their work functions. Surface potential analysis demonstrated that the work function of {010} +  $\text{O}_\text{N}$  and {001} +  $\text{O}_\text{N}$  surfaces is about 3.86 and 5.34 eV, respectively, both them are lower than 6.28 eV for clean {010} and 5.55 eV for clean {001} surface (Fig. 5b–e), resulting from their inherent differences in atomic

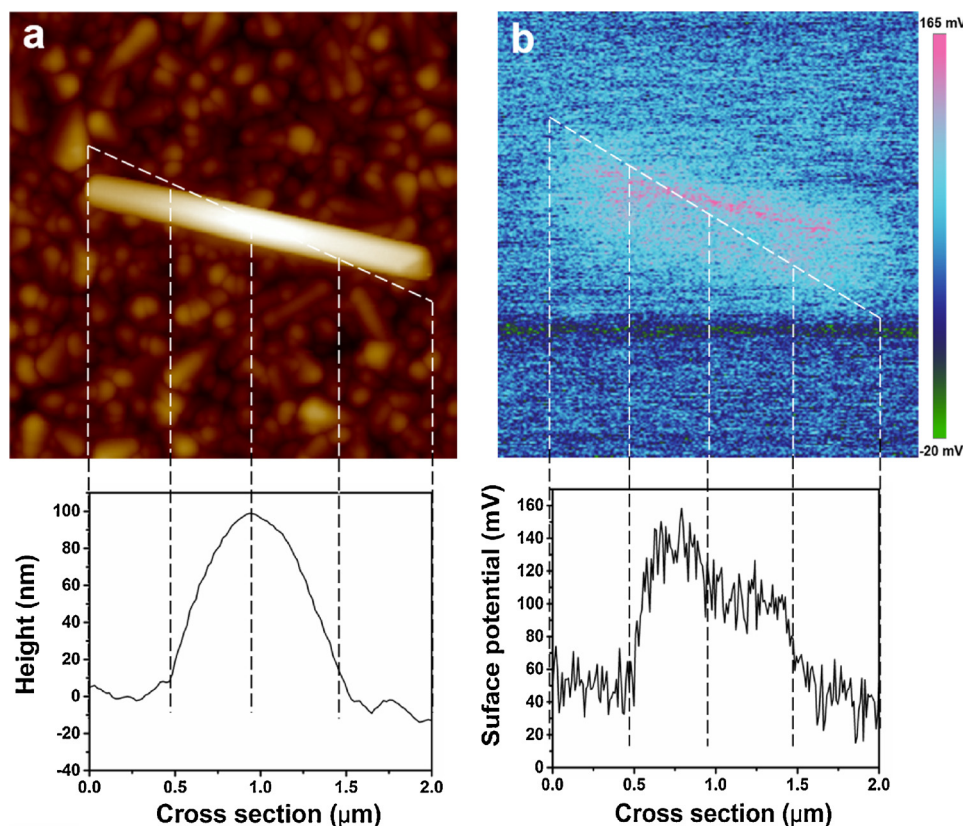


**Fig. 4.** (a) Topographic image of single  $\text{Ta}_3\text{N}_5$  cuboid on FTO substrate. (b) The surface potentials were shown in color scale, and the pink regions represent the higher surface potential.

construction. Given that Fermi level position of bulk  $\text{Ta}_3\text{N}_5$  is near  $-4.15$  eV [49], the surface band bending upward was formed at interface between both  $\{010\}$  and  $\{001\}$  surfaces and the bulk for thermodynamic equilibrium, similar to the formation of Schottky junction. After introduction of  $\text{O}_\text{N}$ , such a band bending originated from difference in surface-bulk work function and can also be achieved at interface region between  $\{001\} + \text{O}_\text{N}$  surface and bulk. In contrast, the work

function of  $\{010\} + \text{O}_\text{N}$  is much close to that of bulk  $\text{Ta}_3\text{N}_5$ , suggesting that there is no obvious space charge region on the surface of  $\{010\} + \text{O}_\text{N}$ . A facet with higher work function would induce a bigger surface band bending due to that exposed facets would share the same bulk Fermi level. Therefore, we believe that band bending upward of  $\{001\}$  facet is much higher than that of  $\{010\}$  facet due to its high work function, that is, a more striking built-in electric field in space charge

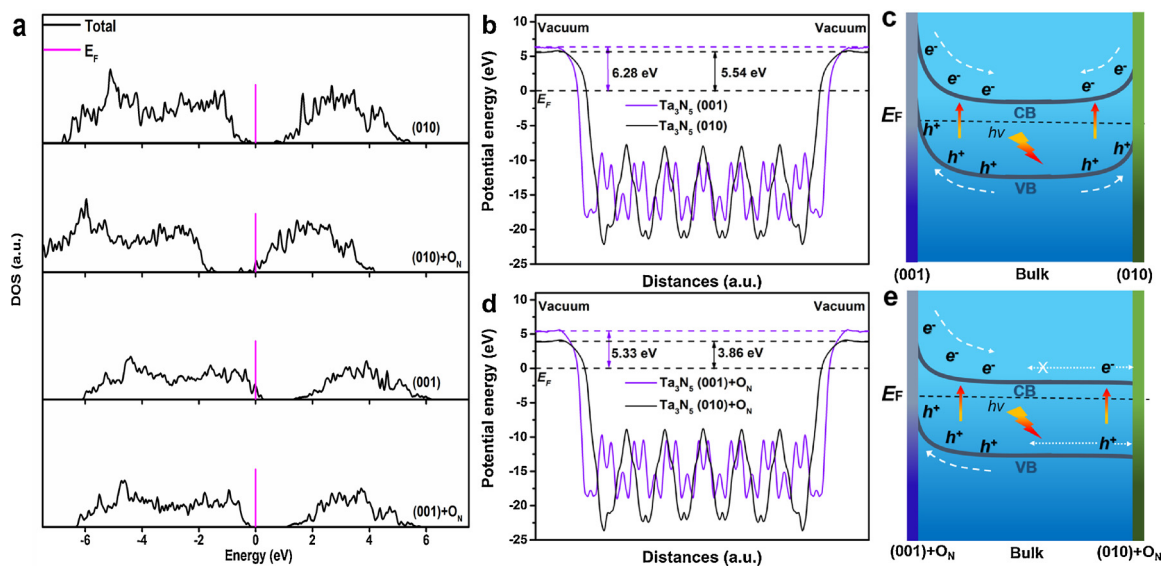


**Fig. 5.** (a) Theoretical calculated density of states (DOS) plots for  $\{010\}$ ,  $\{001\}$ ,  $\{010\} + \text{O}_\text{N}$  and  $\{001\} + \text{O}_\text{N}$  surfaces of  $\text{Ta}_3\text{N}_5$ . (b) Potential diagrams of  $\{010\}$  and  $\{001\}$  surface based on the first-principles simulation ( $E_\text{F}$  denotes the Fermi level). (c) Schematic diagram of the surfaces band bending in the ideal case of clean surface model. (d) Potential diagrams of  $\{010\} + \text{O}_\text{N}$  and  $\{001\} + \text{O}_\text{N}$  surfaces based on the first-principles simulation. (e) Schematic diagram of the surface band bending on the  $\{010\} + \text{O}_\text{N}$  and  $\{001\} + \text{O}_\text{N}$  surfaces.



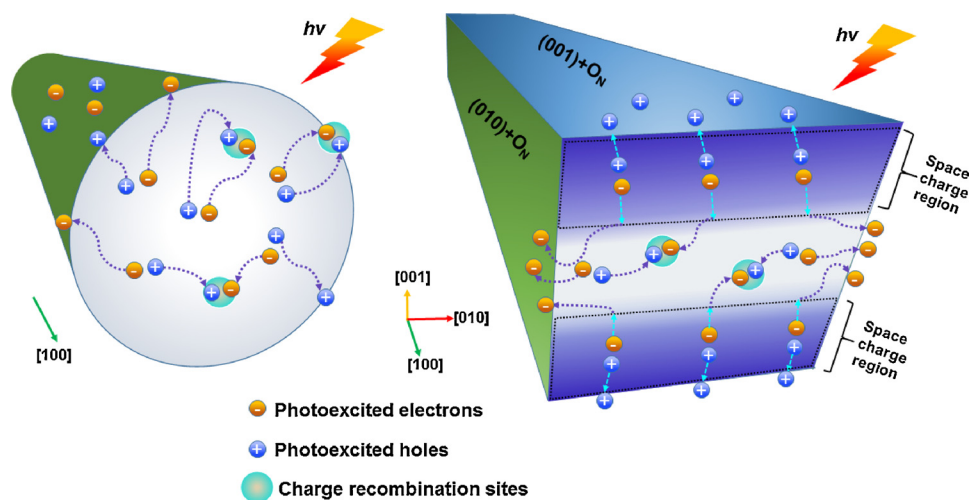


**Fig. 6.** A scheme to describe the behaviors of carriers migration in  $\text{Ta}_3\text{N}_5$  nanorod and effect of electric field region on  $\text{Ta}_3\text{N}_5$  cuboid contributing the spatial charge separation.

region beneath {001} facet drives the directional hole accumulation on {001} surface and the electron drift toward its adjacent {010} surface. A small band bending upward for {010} surface will be easily flattened by photoelectrons generated under illumination, and the photoelectrons from space charge region of {001} facet would further enlarge the effect of flattening band bending, thus benefiting to the electron accumulation on {010} surface. Obviously, such a directional charge transfer from {001} +  $\text{O}_\text{N}$  to {010} +  $\text{O}_\text{N}$  is more easy to realize, owing to no obvious barrier on the {010} +  $\text{O}_\text{N}$  facet to hinder the migration of electrons. This means that the oxygen defects provide a positive effect to the spatial separation of charges. In contrast,  $\text{Ta}_3\text{N}_5$  nanorod without exposed specific facets would exhibit no obvious difference in its surface band bending, even the surface oxygen defects were introduced (Fig. 6).

Fig. 7a and b show the time course of  $\text{CH}_4$  generation over various  $\text{Ta}_3\text{N}_5$  samples. The photocatalytic activities of  $\text{Ta}_3\text{N}_5$  cuboids remain almost unchanged after four reaction cycles, whereas the  $\text{Ta}_3\text{N}_5$  nanorods and particles can only maintain 63% and 60% of their initial performances at third cycle. And the 2:1 M ratio of  $\text{O}_2$  to  $\text{CH}_4$  was well kept for each cycling reaction. XPS analysis was employed to further investigate the surface chemical states of the three samples after photoreduction reaction. As shown in Fig. 7c and S1b, for both  $\text{Ta}_3\text{N}_5$  nanorods and particles, the relative intensity of the Ta 4p peaks increased after illumination while intensity of the N1 s peak decreased. The N/Ta changes in XPS spectra indicated that the  $\text{Ta}_3\text{N}_5$  nanorods and particles suffer from severe self-oxidation process by photogenerated holes which are not delivered to the surface of catalyst in time to participate in the photocatalytic reaction. As for  $\text{Ta}_3\text{N}_5$  cuboids, the formed built-in electric field beneath (001) +  $\text{O}_\text{N}$  facet drives the hole migration from bulk to surface fast, which effectively limits this self-oxidation process. The (010) +  $\text{O}_\text{N}$  and (001) +  $\text{O}_\text{N}$  facets have different work functions, which means that Pt deposition on different crystal faces will affect the electron behavior of metal-semiconductor interfaces. The Pt particles (3Wt%) were also deposited on the surface of  $\text{Ta}_3\text{N}_5$  by impregnation approach that normally results in random dispersion [24,27]. Compared with the  $\text{Ta}_3\text{N}_5$  particles and nanorods, the photocatalytic activity in Fig. 7d is obviously decreased when the Pt cocatalyst was randomly deposited on the crystal facets of  $\text{Ta}_3\text{N}_5$  cuboids. Actually, when the work function of a metal is greater than that of an n-type semiconductor, a Schottky junction can be established after close metal-semiconductor contact, and accelerates effectively the transfer of electrons from the semiconductor to the metal [29]. As seen in Fig. 7e, the potential of Pt is approximately 1.8 V lower than that of  $\text{Ta}_3\text{N}_5$  (010) +  $\text{O}_\text{N}$  facet and close to that of  $\text{Ta}_3\text{N}_5$  (001) +  $\text{O}_\text{N}$  facet, which means that the n-type Schottky junction can be constructed to accelerate the

transfer of photogenerated electrons at  $\text{Ta}_3\text{N}_5$  (010) +  $\text{O}_\text{N}$ -Pt interface rather than  $\text{Ta}_3\text{N}_5$  (001) +  $\text{O}_\text{N}$ -Pt interface (Fig. 7f). Therefore, the  $\text{CO}_2$  reduction activities of  $\text{Ta}_3\text{N}_5$  cuboids with different deposition method of Pt cocatalyst show significant differences, which exactly proves the above-mentioned theoretical simulations.

Although the significant difference in surface band bending is greatly contributing to the enhancement in charge separation, the directional charge transfer behavior may induce an undesirable back electron transfer in an electrode that was composed of randomized  $\text{Ta}_3\text{N}_5$  cuboids. A single-particle electrode model was adopted for easily understanding. As shown in Fig. S16, owing to the geometric symmetry of electron or hole gathering surface on  $\text{Ta}_3\text{N}_5$  cuboid, if an electron gathering surface of the  $\text{Ta}_3\text{N}_5$  cuboid contacted with the FTO conductive substrate, electron transfer from semiconductor to FTO will not be hindered. On the contrary, the electron transfer is restricted when a hole gathering surface contacted with the FTO substrate, which may induce a portion of electrons to migrate to the lateral surface of the cuboid to participate in an undesirable reduction reaction. Both the two electron transfer processes randomly existed in the  $\text{Ta}_3\text{N}_5$  cuboids electrode. Indeed, a significant cathodic current on  $\text{Ta}_3\text{N}_5$  cuboids electrode was observed at a wide applied potential range of 0.6–1.2  $\text{V}_{\text{RHE}}$  (Fig. 2b, c), which may indicate that a small portion of the electrons is not readily transferred to the FTO but involved in a oxygen reduction reaction (Fig. S16).

#### 4. Conclusions

In summary, the [100] crystal-oriented  $\text{Ta}_3\text{N}_5$  cuboids with dominant coexposed {010} and {001} lateral plane was prepared by nitriding reaction with assistance of molten salts and exhibited a significant improvement in photoreduction of  $\text{CO}_2$  and photoelectrochemical water splitting. Exposing {001} facets with high work function on  $\text{Ta}_3\text{N}_5$  cuboid to induce a significant surface band bending, and transferring charges along brachydiagonal direction were effectively to facilitate the spatial separation of photoinduced charges. This work may provide a new strategy for developing more efficient transition metal nitride photocatalysts with visible light absorption based on semiconductor nanocrystal engineering.

#### Conflict of interest

The authors declare no competing financial interest.

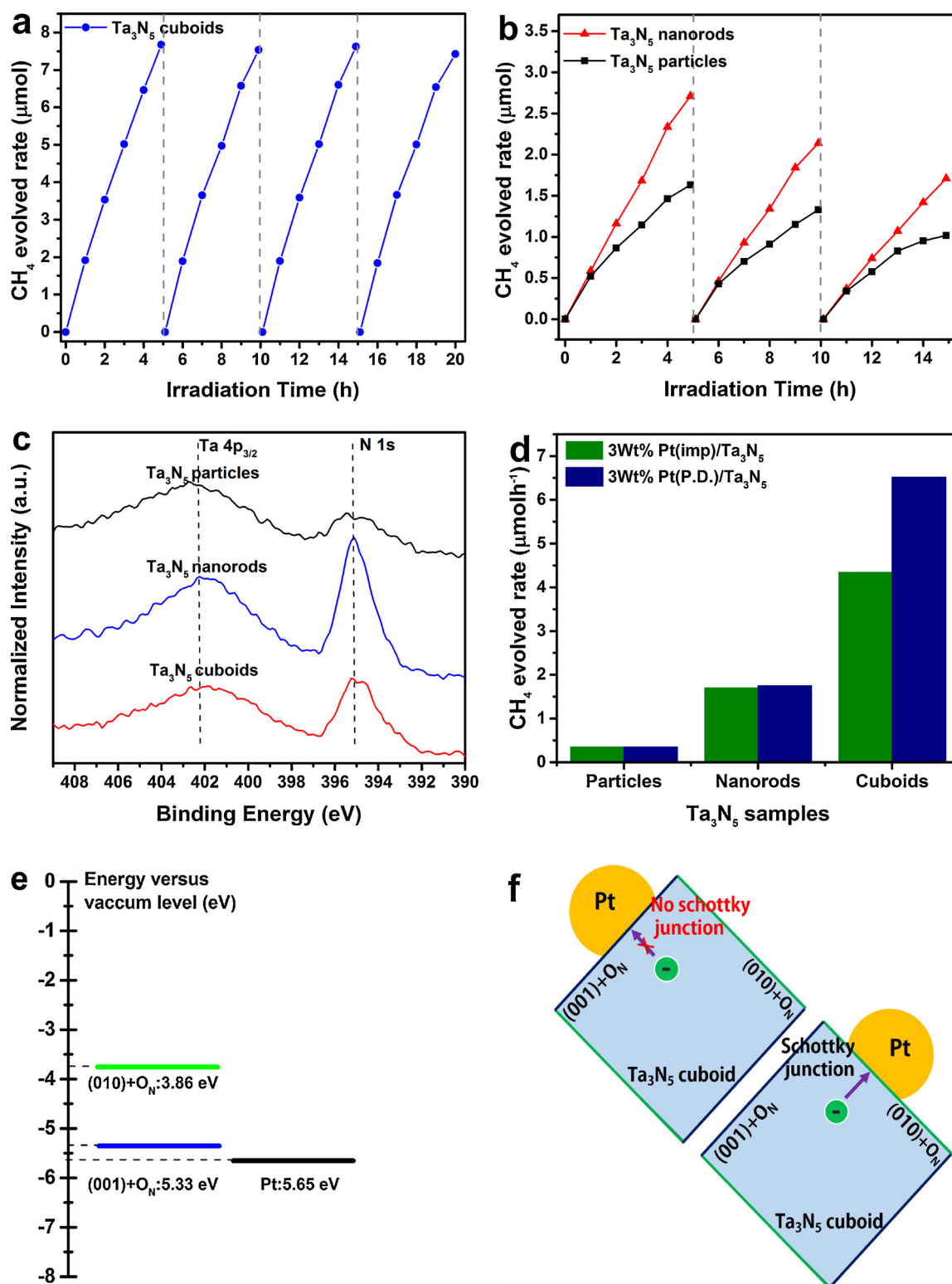


**Fig. 7.** Time course of CH<sub>4</sub> evolution under irradiation of a 300 W Xe lamp ( $\lambda \geq 420$  nm) over (a) Ta<sub>3</sub>N<sub>5</sub> cuboids, (b) Ta<sub>3</sub>N<sub>5</sub> nanorods and particles. (c) Ta 4p and N 1 s XPS spectra of Ta<sub>3</sub>N<sub>5</sub> samples after illumination for 14 h. (d) CH<sub>4</sub> generation over Ta<sub>3</sub>N<sub>5</sub> samples with loading of 3Wt% Pt (Impregnation method noted as Pt (imp)/Ta<sub>3</sub>N<sub>5</sub> and photodeposition method noted as Pt(P.D.)/Ta<sub>3</sub>N<sub>5</sub>). (e) Surface potential positions of Ta<sub>3</sub>N<sub>5</sub> (001) + O<sub>N</sub> and (010) + O<sub>N</sub> and the Fermi level position of Pt. (f) Illustration for the charge transfer in the cross section of Ta<sub>3</sub>N<sub>5</sub> cuboids with Pt deposited on (001) + O<sub>N</sub> and (010) + O<sub>N</sub> facets.

## Acknowledgements

This work was supported primarily by the National Basic Research Program of China (2013CB632404), the National Natural Science Foundation of China (51572121, 21603098 and 21633004), the State

Key Laboratory of NBC Protection for Civilian (SKLNBC2014-09), the Natural Science Foundation of Jiangsu Province (BK20151265, BK20151383 and BK20150580), the Fundamental Research Funds for the Central Universities (021314380084 and 201314380133), the Postdoctoral Science Foundation of China (2017M611784) and the

program B for outstanding PhD candidate of Nanjing University (201702B084). We are grateful to the High Performance Computing Center (HPCC) of Nanjing University for doing the numerical calculations in this paper on its IBM Blade cluster system.

## Appendix A. Supplementary data

Supplementary material related to this article can be found, in the online version, at doi:<https://doi.org/10.1016/j.apcatb.2018.06.036>.

## References

- [1] M. Walter, E. Warren, J. McKone, S. Boettcher, Q. Mi, E. Santori, N. Lewis, *Chem. Rev.* 110 (2010) 6446–6473.
- [2] M. Yan, Y. Hua, F. Zhu, W. Gu, J.H. Jiang, H.Q. Shen, W.D. Shi, *Appl. Catal. B: Environ.* 202 (2017) 518–527.
- [3] C. Li, G. Chen, J. Sun, J.C. Rao, Z.H. Han, Y.D. Hu, W.N. Xing, C.M. Zhang, *Appl. Catal. B: Environ.* 188 (2016) 39–47.
- [4] S. Kohtania, M. Koshiko, A. Kudo, K. Tokumura, Y. Ishigaki, A. Toriba, K. Hayakawa, R. Nakagaki, *Appl. Catal. B: Environ.* 46 (2003) 573–586.
- [5] Z. Zou, J. Ye, K. Sayama, H. Arakawa, *Nature* 414 (2001) 625–627.
- [6] P. Zhang, J. Zhang, J. Gong, *Chem. Soc. Rev.* 43 (2014) 4395–4422.
- [7] M. Liao, J. Feng, W. Luo, Z. Wang, J. Zhang, Z. Li, T. Yu, Z. Zou, *Adv. Funct. Mater.* 22 (2012) 3066–3074.
- [8] M. Li, W. Luo, D. Cao, X. Zhao, Z. Li, T. Yu, Z. Zou, *Angew. Chem. Int. Ed.* 52 (2013) 11016–11020.
- [9] K. Ueda, T. Minegishi, J. Clune, M. Nakabayashi, T. Hisatomi, H. Nishiyama, M. Katayama, N. Shibata, J. Kubota, T. Yamada, K. Domen, *J. Am. Chem. Soc.* 137 (2015) 2227–2230.
- [10] J. Morber, I. Narkeviciute, T. Jaramillo, G. Galli, *Phys. Rev. B* 90 (2014) 155204–155214.
- [11] A. Ziani, E. Nurlaela, D. Dhawale, D. Silva, E. Alarousa, O. Mohammed, K. Takanabe, *Phys. Chem. Chem. Phys.* 17 (2015) 2670–2677.
- [12] A. Ishikawa, T. Takata, J. Kondo, M. Hara, K. Domen, *J. Phys. Chem. B* 108 (2004) 11049–11053.
- [13] S. Li, J. Zhang, S. Hu, K. Xu, W. Jing, J. Liu, *J. Alloys Compd.* 695 (2017) 1137–1144.
- [14] Z. Wang, J. Hou, S. Jiao, K. Huang, H. Zhu, *J. Mater. Chem.* 22 (2012) 21972–21978.
- [15] I. Narkeviciute, P. Chakthranout, A. Mackus, C. Hahn, B. Pinaud, S. Bent, T. Jaramillo, *Nano Lett.* 16 (2016) 7565–7572.
- [16] S. Ma, K. Maeda, T. Hisatomi, M. Tabata, A. Kudo, K. Domen, *Chem. Eur. J.* 19 (2013) 7498–7486.
- [17] M. Zhong, T. Hisatomi, Y. Sasaki, S. Suzuki, K. Teshima, M. Nakabayashi, N. Shibata, H. Nishiyama, M. Katayama, T. Yamada, K. Domen, *Angew. Chem. Int. Ed.* 56 (2017) 4739–4743.
- [18] G. Liu, J. Shi, F. Zhang, Z. Chen, J. Han, C. Ding, S. Chen, Z. Wang, H. Han, C. Li, *Angew. Chem. Int. Ed.* 53 (2014) 7295–7299.
- [19] G. Fu, S. Yan, T. Yu, Z. Zou, *Appl. Phys. Lett.* 107 (2015) 171902–171908.
- [20] E. Nurlaela, M. Harb, S. del Gobbo, M. Vashishta, K. Takanabe, *J. Solid State Chem.* 229 (2015) 219–227.
- [21] H. Tong, S. Ouyang, Y. Bi, N. Umezawa, M. Oshikiri, J. Ye, *Adv. Mater.* 24 (2012) 229–251.
- [22] J. Yu, J. Low, W. Xiao, P. Zhou, M. Jaroniec, *J. Am. Chem. Soc.* 136 (2014) 8839–8842.
- [23] X. Liu, G. Dong, S. Li, G. Lu, Y. Bi, *J. Am. Chem. Soc.* 138 (2016) 2917–2920.
- [24] R. Li, F. Zhang, D. Wang, J. Yang, M. Li, J. Zhu, X. Zhou, H. Han, C. Li, *Nat. Commun.* 4 (2013) 1432–1441.
- [25] J. Zhu, F. Fan, R. Chen, H. An, Z. Feng, C. Li, *Angew. Chem. Int. Ed.* 54 (2015) 9111–9242.
- [26] R. Li, H. Han, F. Zhang, D. Wang, C. Li, *Energy Environ. Sci.* 7 (2014) 1369–1376.
- [27] L. Mu, Y. Zhao, A. Li, S. Wang, Z. Wang, J. Yang, Y. Wang, T. Liu, R. Chen, J. Zhu, F. Fan, R. Li, C. Li, *Energy Environ. Sci.* 9 (2016) 2463–2469.
- [28] P. Li, Y. Zhou, Z. Zhao, Q. Xu, X. Wang, M. Xiao, Z. Zou, *J. Am. Chem. Soc.* 137 (2015) 9547–9550.
- [29] L. Wang, J. Ge, A. Wang, M. Deng, X. Wang, S. Bai, R. Li, J. Jiang, Q. Zhang, Y. Luo, Y. Xiong, *Angew. Chem. Int. Ed.* 53 (2014) 5107–5211.
- [30] H. Yang, C. Sun, S. Qiao, J. Zou, G. Liu, S. Smith, H. Cheng, G. Lu, *Nature* 453 (2008) 638–641.
- [31] S. Ma, T. Hisatomi, K. Maeda, Y. Moriya, K. Domen, *J. Am. Chem. Soc.* 134 (2012) 19993–19996.
- [32] Y. He, J. Thorne, C. Wu, P. Ma, C. Du, Q. Dong, J. Guo, D. Wang, *Chem* 1 (2016) 640–655.
- [33] L. Wang, X. Zhou, N. Nguyen, I. Hwang, P. Schmuki, *Adv. Mater.* 28 (2016) 2432–2438.
- [34] M. Xiao, B. Luo, M. Lyu, S. Wang, L. Wang, *Adv. Energy Mater.* 17 (2017) 1605–1608.
- [35] Y. Li, L. Zhang, A. Torres-Pardo, J.M. González-Calbet, Y. Ma, P. Oleynikov, O. Terasaki, S. Asahina, M. Shima, D. Cha, L. Zhao, K. Takanabe, J. Kubota, K. Domen, *Nat. Commun.* 4 (2013) 1–7.
- [36] S. Suzuki, K. Teshima, K. Yubuta, S. Ito, Y. Moriga, T. Takata, T. Shishido, K. Domen, *CrystEngComm* 14 (2012) 7178–7183.
- [37] S. Suzuki, H. Wagata, M. Komatsus, T. Minegishi, K. Domen, S. Oishi, K. Teshima, *J. Mater. Chem. A* 3 (2015) 13946–13952.
- [38] D. Lu, M. Hara, T. Hisatomi, T. Takata, K. Domen, *J. Phys. Chem. C* 113 (2009) 17151–17155.
- [39] S. Chen, S. Shen, G. Liu, Y. Qi, F. Zhang, C. Li, *Angew. Chem. Int. Ed.* 54 (2015) 3047–3051.
- [40] S. Yan, S. Ouyang, J. Gao, M. Yang, J. Feng, X. Fan, L. Wan, Z. Li, J. Ye, Y. Zhou, Z. Zou, *Angew. Chem. Int. Ed.* 122 (2010) 6544–6549.
- [41] M. Tahir, N.S. Amin, *Sustain. Energy Rev.* 25 (2013) 560–579.
- [42] M.S. Hamdy, R. Amrollahi, I. Sinev, B. Mei, G. Mul, *J. Am. Chem. Soc.* 136 (2014) 594–597.
- [43] S. Gao, Y. Lin, X. Jiao, Y. Sun, Q. Luo, W. Zhang, D. Li, J. Yang, Y. Xie, *Nature* 529 (2016) 68–71.
- [44] M. Higashi, K. Domen, R. Abe, *Energy Environ. Sci.* 4 (2011) 4138–4147.
- [45] H. Li, Y. Gao, Y. Zhou, F. Fan, Q. Han, Q. Xu, X. Wang, M. Xiao, C. Li, Z. Zou, *Nano Lett.* 16 (2016) 5547–5552.
- [46] M. Ritala, P. Kalsi, D. Riihela, K. KuKli, M. Leskela, J. Jokinen, *J. Chem. Mater.* 11 (1999) 1712–1718.
- [47] S. Henderson, A. Hector, *J. Solid State Chem.* 179 (2006) 3518–3524.
- [48] J. Wang, J. Feng, L. Zhang, Z. Li, Z. Zou, *Phys. Chem. Chem. Phys.* 16 (2014) 15375–15380.
- [49] W. Chun, A. Ishikawa, H. Fujisawa, T. Takata, J. Kondo, M. Hara, M. Kawai, Y. Matsumoto, *J. Phys. Chem. B* 107 (2003) 1798–1803.